

Vibrational Coupling Infrared Nanocrystallography

Richard L. Puro, Thomas P. Gray, Tsitsi A. Kapfunde, George B. Richter-Addo, and Markus B. Raschke*



Cite This: <https://doi.org/10.1021/acs.nanolett.3c03958>



Read Online

ACCESS |

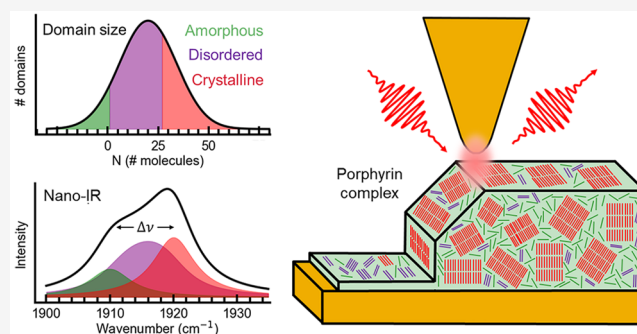
Metrics & More

Article Recommendations

Supporting Information

ABSTRACT: Coupling between molecular vibrations leads to collective vibrational states with spectral features sensitive to local molecular order. This provides spectroscopic access to the low-frequency intermolecular energy landscape. In its nanospectroscopic implementation, this technique of vibrational coupling nanocrystallography (VCNC) offers information on molecular disorder and domain formation with nanometer spatial resolution. However, deriving local molecular order relies on prior knowledge of the transition dipole magnitude and crystal structure of the underlying ordered phase. Here we develop a quantitative model for VCNC by relating nano-FTIR collective vibrational spectra to the molecular crystal structure from X-ray crystallography. We experimentally validate our approach at the example of a metal organic porphyrin complex with a carbonyl ligand as the probe vibration. This framework establishes VCNC as a powerful tool for measuring low-energy molecular interactions, wave function delocalization, nanoscale disorder, and domain formation in a wide range of molecular systems.

KEYWORDS: vibrational exciton, transition dipole coupling, infrared spectroscopy, scattering scanning near-field optical microscopy (s-SNOM), crystallography



Many macroscopic functional properties of molecular materials are sensitive to the local microscopic environment seen by each molecule. Intermolecular coupling of excitons and nanoscale structure influence the photonic and electronic performance of optoelectronic systems, as well as the functionality of proteins and other biological systems.^{1–4} Similarly, intermolecular coupling of vibrations is important in determining energy and charge transfer on molecular length scales.^{5–10} Coupling leads to the emergence of collective vibrations and the delocalization of the vibrational wave function across neighboring molecules,^{11,12} with associated changes to vibrational spectra. Eigenmode energies will shift or split depending on the distance, magnitude, and relative orientation of infrared (IR) transition dipoles.^{13,14} On one hand, this can lead to seemingly anomalous changes to lineshapes and mode energies in IR vibrational spectroscopy,^{15,16} changes to Raman scattering energies or even Raman selection rules,^{17–19} and potential complications in the interpretation of vibrational spectra.^{20–22} On the other hand, the orientation-dependent spectral features of collective vibrations can be used as a tool to measure local molecular order, disorder, and crystallinity as established only recently.^{13,14,23}

Due to the interactions between vibrational transition dipoles, accurate interpretation of spectral features in dense molecular systems, such as liquids²¹ or solids,^{11,24} relies on modeling. This is commonly performed by calculating the collective eigenmodes that arise from transition dipole

coupling for the vibrations of interest.^{11,12,24–30} Because of the similarity between the mathematical description of vibrational transition dipole coupling and excitonic dipole coupling, this treatment has conventionally been referred to as the vibrational exciton model (VEM).¹¹

The VEM has been applied to IR spectroscopy of, e.g., proteins to noninvasively measure their secondary or tertiary structure^{26–28,31,32} and molecular aggregates to track crystallization and phase changes over time.^{24,25,30,33} Raman spectra are also modified by transition dipole coupling, which was demonstrated in surface-enhanced Raman scattering (SERS) of molecular monolayers where collective frequency shifts induced by coupling were related to chemical reaction kinetics.¹⁸ Recently, transition dipole interactions have been probed in small ensembles of molecules by applying the VEM to IR nanoimaging.^{13,14,23} This extension of IR vibrational coupling spectroscopy to nanoimaging has established a new technique of all-optical vibrational coupling nanocrystallography (VCNC), which complements established X-ray and electron based crystallography with its sensitivity to defects and local disorder on the nanoscale.

Received: October 14, 2023

Revised: January 23, 2024

Accepted: January 26, 2024

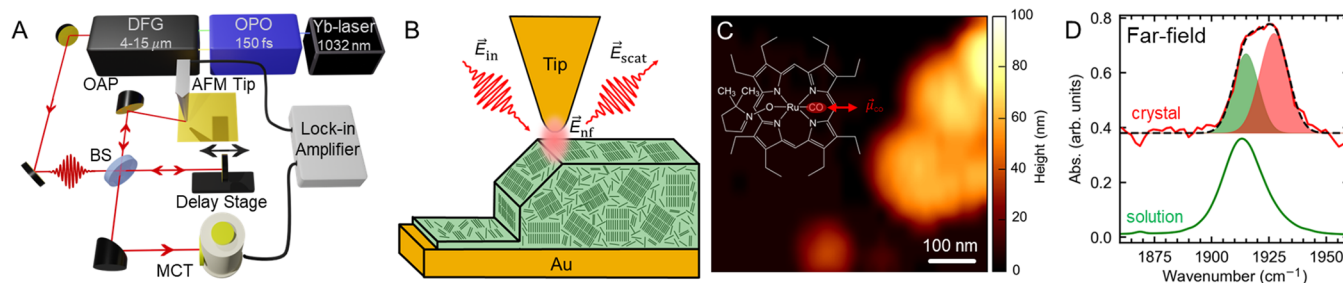


Figure 1. (A) Schematic of nano-FTIR *s*-SNOM.^{35,13} (B) Porphyrin (OEP)Ru(CO)(DMPO) nanocrystal with structural defects and thin amorphous film on a gold substrate. (C) Example AFM topography of (OEP)Ru(CO)(DMPO) nanocrystals. Inset: molecular structure of (OEP)Ru(CO)(DMPO) with a carbonyl ligand as the vibrational probe for vibrational coupling nanocrystallography (VCNC). (D) Far-field IR absorption spectra of (OEP)Ru(CO)(DMPO) nanocrystals measured in reflection micro-FTIR (top) with Gaussian deconvolution into crystalline and amorphous subpopulations (red and green, respectively), and a dilute solution in DCM measured with transmission FTIR (bottom).

Previous VCNC studies were based on a qualitative comparison between measured and modeled vibrational lineshapes with modeling based on assumed crystal structures and transition dipole magnitudes used as fit parameters to derive nanoscale disorder. However, without knowing these transition dipole structural parameters, the underlying vibrational wave function delocalization lengths could not be quantified, leaving an incomplete picture of the accuracy and broader applicability of VCNC. Here we provide a framework for VCNC based on quantitative modeling of collective vibrational spectra using transition dipole structural parameters measured with X-ray diffraction (XRD) and FTIR absorption spectroscopy. The framework is validated at the example of the metal organic porphyrin (OEP)Ru(CO)(DMPO) (OEP = octaethylporphyrinato dianion; DMPO = 5,5-dimethyl-1-pyrroline *N*-oxide) (Figure 1C, inset) as a representative molecular electronic material. We use the carbonyl vibration as a local probe in polycrystalline aggregates of (OEP)Ru(CO)(DMPO), with the magnitude of the vibrational transition dipole and crystal structure of their highly ordered phase as the only input parameters to quantify the vibrational delocalization lengths. This work thus advances infrared nanocrystallography as a precise molecular ruler, complementing corresponding advances in X-ray and electron microscopies.

As established previously,^{11,34} the vibrational exciton Hamiltonian for a system of N vibrations is given by

$$\hat{H} = \sum_i h\nu_i b_i^\dagger b_i + \sum_{i \neq j} V_{ij} (b_i^\dagger b_j + b_j^\dagger b_i) = \begin{pmatrix} h\nu_1 & V_{12} & \dots & V_{1N} \\ V_{21} & h\nu_2 & \dots & V_{2N} \\ \dots & \dots & \dots & \dots \\ V_{N1} & V_{N2} & \dots & h\nu_N \end{pmatrix} \quad (1)$$

where b^\dagger and b are the creation and annihilation operators for vibrational excitations, the diagonal term $h\nu_i$ is the vibrational energy of molecule i (treated as degenerate so that $\nu_1 = \nu_2 = \dots \equiv \nu$), and the off diagonal terms V_{ij} are the interaction energies between vibrations on different molecules, given by

$$V_{ij} = \frac{1}{4\pi\epsilon_0 |\vec{r}_{ij}|^3} \left(\vec{\mu}_i \cdot \vec{\mu}_j - \frac{3(\vec{\mu}_i \cdot \vec{r}_{ij})(\vec{\mu}_j \cdot \vec{r}_{ij})}{|\vec{r}_{ij}|^2} \right) \quad (2)$$

with $\vec{\mu}_i$ being the transition dipole of vibration i and \vec{r}_{ij} being the displacement vector between vibrations i and j . We derive the carbonyl vibrational energy $h\nu$ and transition dipole

magnitude $|\vec{\mu}_{\text{CO}}|$ from IR absorption spectroscopy in dilute solution, and the relative transition dipole positions and orientations \vec{r}_{ij} and $\hat{\mu}_i$ by XRD.

The metalloporphyrin complex (OEP)Ru(II)(CO)-(DMPO) (Figure 1C, inset) was synthesized as described previously.³⁶ We confirm the structure using a single crystal ($\sim 42 \times 60 \times 340 \mu\text{m}^3$), with XRD performed at 100(2) K (D8 Quest κ -geometry diffractometer; Bruker Photon II CMOS area detector; Incoatec $I\mu\text{s}$ microfocus Mo $K\alpha$ source, $\lambda = 0.71073 \text{ \AA}$) (for details, see SI).

IR absorption spectroscopy was performed on solutions of (OEP)Ru(CO)(DMPO) in dichloromethane (DCM), with concentrations ranging from 2.1 to 23 mM, using a commercial FTIR spectrometer (Nicolet iS50 Advanced, Thermo Fisher Scientific) and an IR liquid cell (Pike Technologies) with CaF_2 windows and a 0.1 mm PTFE spacer (Figure 1D, bottom). From the integrated area of the absorption band, expressed as an extinction coefficient $\epsilon(\nu)$ through Beer's Law, the transition dipole magnitude is calculated as^{37,38}

$$|\vec{\mu}| = \sqrt{\frac{3\epsilon_0 h c \ln 10}{2\pi^2 N_A \bar{\nu}} \int \epsilon(\nu) d\nu} \quad (3)$$

with the center frequency of the absorption band $\bar{\nu} = 1911 \text{ cm}^{-1}$ and N_A representing Avogadro's number. The transition dipole moment is found to be $|\vec{\mu}_{\text{CO}}| = (1.43 \pm 0.03) \text{ D}$ (details in SI).

Polycrystalline aggregates of (OEP)Ru(CO)(DMPO) (illustrated in Figure 1B) with heights ranging from hundreds of nanometers (Figure 1C) to several micrometers (not imaged) were deposited from hexane onto a gold substrate by drop casting. IR *s*-SNOM (customized nanoIR2-*s* prototype, Anasys Instruments/Bruker) was performed on these aggregates based on a low-noise tunable femtosecond mid-IR laser source (HarmoniXX difference frequency generation, APE; Levante optical parametric oscillator, APE; Flint Ytterbium pump laser, Light Conversion) with 100 cm^{-1} fwhm bandwidth and 10 mW output power (attenuated to 5 mW) centered at $\lambda = 5.2 \mu\text{m}$ (1920 cm^{-1}), which was focused onto a metallic AFM tip (Pt/Ir coated, ARROW-NCPT-50, NANO World), tapping at a frequency of 250 kHz.

Ten different nanocrystals (C1–C10) were selected for their well-defined topography and studied in spatio-spectral IR *s*-SNOM. We apply the VCNC model directly to the imaginary part of the tip-scattered near-field ($\text{Re}_{\text{NF}} + i \text{Im}_{\text{NF}} = A e^{i\phi}$, as described previously^{35,39}), valid for small phase responses ($\phi_{\text{max}} \lesssim 10^\circ$) for which $\text{Im}_{\text{NF}}(\bar{\nu}) \approx \phi(\bar{\nu}) \approx \kappa$ as is the case

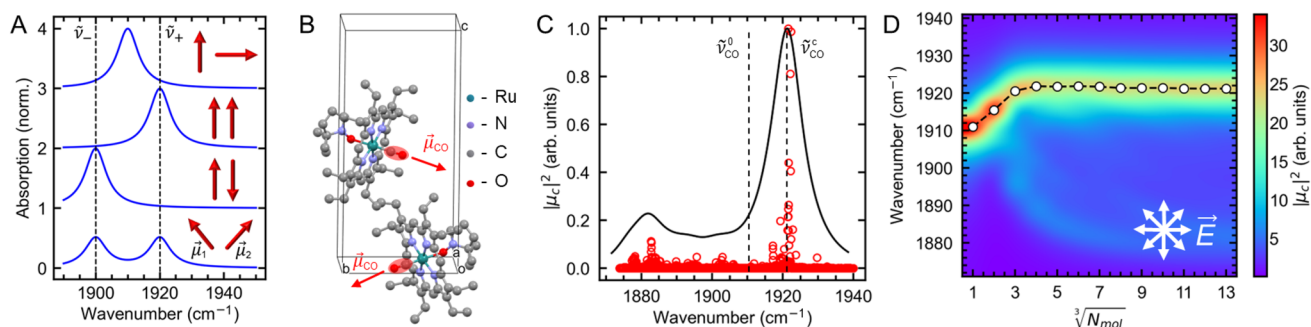


Figure 2. (A) Modeled spectra for dimers with different relative transition dipole orientations. (B) Molecular and crystal structures of DMPO porphyrin with a primitive monoclinic unit cell. The carbonyl ligand is highlighted in red, with arrows denoting the direction of the vibrational transition dipole. (C) Calculated spectrum for a domain with $\sqrt[3]{N} = 13$ molecules. All collective modes (open symbols) result in an emergence of one strongly IR active mode, which is blue-shifted by $\sim 10 \text{ cm}^{-1}$ from the isolated carbonyl vibration (superimposed absorption profile based on Lorentzians with fixed line width of $\Gamma_{\text{FWHM}} = 10 \text{ cm}^{-1}$). (D) Collective frequency shift $\tilde{\nu}_{\text{CO}}$ as a function of domain size ($\sqrt[3]{N}$).

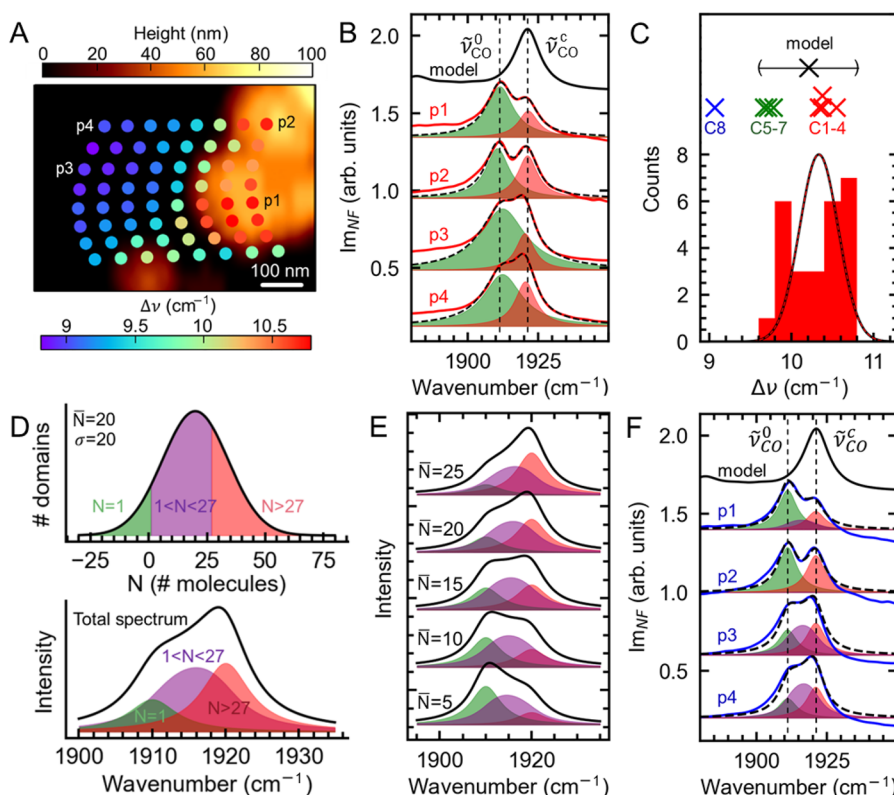


Figure 3. (A) Nano-FTIR imaging of a (OEP)Ru(CO)(DMPO) porphyrin nanocrystal (C1) with spectral shifts of the collective vibrational mode $\Delta\nu$ determined for each point spectrum. (B) Representative point spectra (red) with Lorentzian fits (black, dashed) on more crystalline (p1 and p2) and more amorphous (p3 and p4) regions. (C) Histogram of $\Delta\nu$ measured on polycrystalline aggregate C1 with $\Delta\nu$ for crystals C1–C8 (denoted by "X") compared to modeling. (D) Gaussian domain size distribution model with mean domain size $\bar{N} = 20$ and standard deviation $\sigma_N = 20$ deconvoluted into domains of single molecules (green), domains with short-range order (purple), and domains with long-range order (red) (top). Corresponding spectrum with respective domain contributions (bottom). (E) Spectral evolution as a function of \bar{N} with $\sigma_N = 20$ fixed. (F) Gaussian model fit to spectra from (B) with corresponding spectral deconvolution (for details, see SI).

here. For larger phase responses, various models to account for the extrinsic tip–sample coupling could be applied.^{39,40}

Figure 1D shows representative micro-FTIR spectra of (OEP)Ru(CO)(DMPO) crystallites in the carbonyl spectral region (top; Nicolet Continuum, Thermo Fisher) in comparison to a solution spectrum (bottom). From a Gaussian deconvolution, it is seen that crystalline (OEP)Ru(CO)(DMPO) exhibits both a peak at $\sim 1911 \text{ cm}^{-1}$ and a blue-shifted peak. We attribute the higher energy peak to the collective carbonyl vibrations from molecules in a crystalline

phase and the lower energy peak to uncoupled carbonyl vibrations from molecules in an amorphous phase, corresponding to the solution spectrum of isolated molecules.

To predict the collective vibrational spectrum of the porphyrin crystals as a function of crystalline domain size, we diagonalize eq 1 numerically to find the eigenenergies and dipole moments of the collective modes for varying values of N . The carbonyl atom positions in the two molecules within a unit cell are used to define the positions and relative orientations of the vibrational dipoles. With these coordinates,

we construct crystalline domains approximated as equilateral parallelepipeds.

For the polycrystalline aggregates, we expect to measure a polarization-averaged collective spectrum. For a single crystal, only modes with transition dipoles oriented along the tip axis would contribute to the measured spectrum (see SI for the polarization dependence). The calculated polarization-averaged collective energy spectrum for a crystalline ensemble of ~ 2200 molecules ($\sqrt[3]{N} = 13$ molecules per side, representative of the $N \rightarrow \infty$ limit) is shown in Figure 2C, with the uncoupled carbonyl vibration at $\tilde{\nu}^0 = 1911 \text{ cm}^{-1}$. The spectrum is dominated by a minority of collective modes, with strong IR activity centered at $\tilde{\nu}^c = 1921 \text{ cm}^{-1}$. For reasons of symmetry, most collective modes have low or negligible IR activity. Modeled spectra are generated by superimposing Lorentzian absorption profiles for each collective mode with a fixed line width of $\Gamma_{FWHM} = 10 \text{ cm}^{-1}$ (black solid).

The center frequency of the collective mode is dependent on the number of interacting molecules in each domain N . Figure 2D shows the spectral evolution as a function of $\sqrt[3]{N}$ with $|\bar{\mu}_{CO}| = 1.43 \text{ D}$. It can be seen that the dominant IR-active collective mode at $\tilde{\nu}^c \sim 1921.2 \text{ cm}^{-1}$ (corresponding to a frequency shift from the uncoupled mode of $\Delta\tilde{\nu}_{\text{mod}} = 10.2 \text{ cm}^{-1}$) rapidly converges already for $\sqrt[3]{N} \geq 3$ with an uncertainty in the large domain limit of $\sigma_N = 0.4 \text{ cm}^{-1}$. In general, a more continuous shift up to larger values of N is ideal for the VCNC to resolve variations in domain size over a longer range. A nearly constant coupled mode frequency for $\sqrt[3]{N} \geq 3$ limits the utility of transition dipole coupling as a molecular ruler for imaging domain size. For this model study, however, the negligible dependence of $\tilde{\nu}^c$ on N is desirable for comparison between modeling and experimental results, since the exact domain sizes within the tip near-field are unknown.

The uncertainty σ_N together with the uncertainty in $|\bar{\mu}_{CO}|$ of $\pm 0.03 \text{ D}$, which translates to an uncertainty in $\Delta\tilde{\nu}_{\text{mod}}$ of $\sigma_\mu = 0.4 \text{ cm}^{-1}$ (see SI), leads to a combined uncertainty in $\Delta\tilde{\nu}_{\text{mod}}$ of 0.6 cm^{-1} , or 6% of the expected energy shift. The expected collective mode shift of $\Delta\tilde{\nu}_{\text{mod}} = 10.2 \pm 0.6 \text{ cm}^{-1}$ can now be compared to measured shifts to determine the deviation between modeling and experiment.

To this end, we perform spatio-spectral IR s -SNOM and extract $\Delta\tilde{\nu}$ for point spectra measured on selected polycrystalline aggregates. Figure 3A shows the locations of the point spectra measured on crystal aggregate C1 and on an adjacent region with flat topography. Spectra are fit using a superposition of two Lorentzian absorption profiles, with examples shown in Figure 3B (data red solid, fits dashed black). Symbols in Figure 3A represent the resulting frequency shift, $\Delta\tilde{\nu}$, between the collective and uncoupled mode frequencies. All points on the aggregate exhibit a value of $\Delta\tilde{\nu} \gtrsim 10 \text{ cm}^{-1}$, with similar results obtained for other aggregates, summarized as a histogram in Figure 3C. The average value of $\Delta\tilde{\nu} = 10.3 \pm 0.3 \text{ cm}^{-1}$ is in good agreement with the modeled value of $\Delta\tilde{\nu}_{\text{mod}} = 10.2 \pm 0.6 \text{ cm}^{-1}$.

In contrast, nano-FTIR spectra of the flat region adjacent to the aggregate also exhibit a collective vibrational response but with a smaller frequency shift of $\Delta\tilde{\nu} \approx 9 \text{ cm}^{-1}$. We interpret this region as a mostly amorphous thin film of (OEP)Ru(CO)(DMPO) deposited along with the aggregates during drop casting (illustrated in Figure 1B). Such regions would likely form small crystalline domains composed of few molecules. In this case, the well-defined crystalline peak may

arise from a minority of domains larger than $\sqrt[3]{N} = 3$ ($N > 27$), while smaller domains would contribute to a broadened background response, distorting the profiles of large domains and domains of isolated molecules.

For these predominantly amorphous regions, we treat the collective vibrational spectra as a superposition of domains assuming a normal distribution of domain sizes with variable average \bar{N} and standard deviation σ_N (Figure 3D, top). Fully disordered domains ($N \leq 1$, green) and domains with long-range order ($N \geq 27$, red) are represented by Lorentzian profiles with center frequencies 1911 and 1921.2 cm^{-1} , respectively. The intermediate domain responses ($1 < N < 27$, purple) are approximated with $\bar{\nu}$ shifting linearly between these two frequencies. The resulting spectrum (Figure 3D, bottom) is then the superposition of these three regions of domain sizes. Resulting model spectra and their domain decompositions are shown in Figure 3E for fixed $\sigma_N = 20$ and varying \bar{N} . We observe a transition from an amorphous to crystalline dominated spectral response with increasing \bar{N} .

We apply this model to points p1–p4 to separate the contributions of fully disordered, partially crystalline, and bulk crystalline domains from the measured spectra (Figure 3F). Spectra are fit by varying only \bar{N} and σ_N . For points p1 and p2, the intermediate domains do not contribute notably to the response, in contrast to points p3 and p4 with corresponding fit parameters $\bar{N} = 16$ and 18 and $\sigma_N = 23$ and 20 , respectively. These results suggest that spectra from regions composed of mostly intermediate domains materialize in a similar way to domains composed of two distinct Lorentzian responses but with narrowed peak splitting.

Additional nano-FTIR spectra of other polycrystalline aggregates (C2–C8) exhibit a similar blue-shifted collective peak spectrally resolved from the uncoupled molecular response. Only two aggregates (C9 and C10) exhibit a purely uncoupled carbonyl response (see Figure S3). Collective mode frequency shifts are consistently below 10.6 cm^{-1} (Figure 3C, top), in agreement with modeling. The seven aggregates C1–C7 exhibit values of $\Delta\tilde{\nu}$ within the model uncertainty (within 6% of $\Delta\tilde{\nu}_{\text{mod}} = 10.2 \text{ cm}^{-1}$). Crystal C8 exhibits a much lower value of $\Delta\tilde{\nu} \approx 9 \text{ cm}^{-1}$ like the amorphous film region adjacent to aggregate C1. Fits of the Gaussian domain size distribution model to crystal spectra of C5–C8 are shown in the SI and suggest that contributions from intermediate domains are the reason for the narrowed splitting compared to crystals C1–C4. Overall, we find good agreement between VCNC modeling with minimal free parameters and nano-FTIR spectra measured on a range of amorphous and crystalline aggregates.

The porphyrin molecules studied in this work were selected because they crystallize in a lattice that leads to a rapid asymptote of the collective frequency shift. Broader applications of VCNC as a molecular ruler to study order and disorder require a gradual collective mode frequency shift over a larger range of N values, since changes in domain size are not resolvable after the collective shift reaches its asymptote. This raises the question of what lattice structural and vibrational dipole parameters define the dynamic range of VCNC. The spectral mode pattern, degree of collective frequency shift, and its length scale cannot be determined intuitively because of the complex superposition of lattice and orientational effects, which require solving the coupling Hamiltonian numerically for a given crystal structure. However, as an example to derive some general trends, we model a simple cubic lattice with

transition dipole orientations shown in Figure 4A. We also model a corresponding 2D lattice.

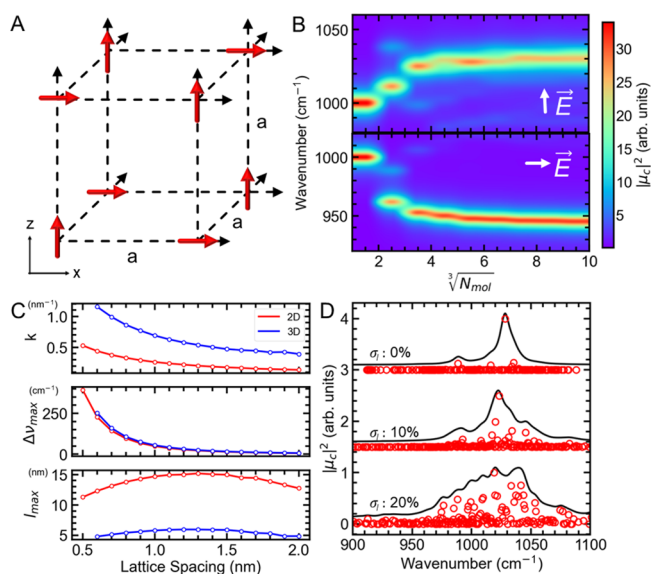


Figure 4. (A) Model structure of transition dipoles arranged in a simple cubic lattice with orientations alternating between the x - and z -axes. (B) Collective vibrational spectra as a function of domain size when probed parallel to the z -axis (top) or x -axis (bottom) for $a = 1$ nm and $|\vec{\mu}| = 2$ D. (C) Rate k , maximum frequency shift $\Delta\nu_{max}$, and maximum resolvable domain size l_{max} as functions of lattice spacing a . (D) Calculated IR spectra (black) and corresponding IR activities of each mode (red) for various degrees of disorder.

Both 3D and 2D lattices exhibit a mode splitting (Figure 4B) and a gradual frequency shift with increasing N . The two modes are orthogonal to one another, with no modes oriented along the y -axis. This is similar to the case of our porphyrin crystal structure, where the blue-shifted collective mode dominates when probing along the crystallographic b -axis, whereas a smaller red-shifted mode appears when probing along the c -axis (see SI). Therefore, in addition to determining disorder and domain size, in polarization studies of single crystals VCNC also allows for determination of crystal orientation.

To determine the effect of lattice spacing and transition dipole magnitude on the dynamic range of VCNC for this model structure, we vary the lattice spacing from 0.6 to 2 nm and the transition dipole magnitude from 0.5 to 2.0 D (typical values for a range of molecules). The dynamic range is quantified by exponential fits to frequency shifts like what is shown in Figure 4B by the decay constant k (nm⁻¹) and the maximum frequency shift $\Delta\nu_{max}$. The maximum resolvable domain size l_{max} is defined as the domain size at which the frequency shift is within 1 cm⁻¹ of $\Delta\nu_{max}$. From the summary of these values for varying 2D and 3D lattice spacing (Figure 4C), we observe a decrease in both k and $\Delta\nu_{max}$ for increasing lattice spacing. These effects compete in their influence on l_{max} to give a peak in the dynamic range for lattice spacings of 1.0 to 1.5 nm. The dynamic range $l_{max} = 10$ –15 nm for the 2D system is much higher than $l_{max} = 5$ –6 nm for the 3D system, facilitating domain size measurements up to 20 molecules.¹³ The corresponding effect of varying transition dipole moment is shown in the SI, where no variation is observed in k but

$\Delta\nu_{max}$ increases with increasing $|\vec{\mu}|$, leading to a monotonic increase in l_{max} with increasing $|\vec{\mu}|$.

Several effects may cause deviations between the measured vibrational response and the response predicted by dipole–dipole interactions modeled here. We approximate the small carbonyl ligand of the otherwise large porphyrin molecule as a simple point dipole and model only the interactions between these dipoles. This simplification neglects the influence of other mobile or polarizable charges,⁴¹ couplings with other vibrational modes,²¹ and higher order multipole interactions.⁴² The presence of free carriers may screen the vibrational dipole field, effectively reducing the transition dipole moment compared to isolated molecules when measured in a weakly polarizable dielectric solvent. This effect may be significant in conjugated π -electron systems, but despite the size and complexity of the porphyrin rings studied here, screening from free electrons appeared to only have a negligible effect, as transition dipole interactions account for most of the collective frequency shift. Higher multipole couplings may become relevant for small molecules or otherwise closely spaced vibrational modes when on the order of the dipole length, i.e., few angstroms. However, these higher order interactions would fall off with separation faster than dipole interactions, meaning that even in systems of very small molecules, higher multipole couplings would likely only be relevant for nearest-neighbor interactions and would cause only an overall shift for larger domains. We expect other solvatochromic effects like a vibrational Stark shift to be negligible in our porphyrin system due to the low polarity and only moderate polarizability of the molecular core, as well as the large separation between polar carbonyl ligands. For highly polar systems, the Stark shift can be included in the vibrational coupling modeling based on, e.g., the Onsager model of solvation.⁴³ However, the expected net overall spectral shift would only minimally depend on molecular disorder as long as the average intermolecular distance is not affected.⁴³

Deviations in the exact transition dipole structural parameters within the crystalline domains can also change the induced frequency shift. We model this effect at the example of the 3D model structure in Figure 4A by adding random static disorder to each structural parameter. As an example, calculated spectra for varying degrees of disorder in transition dipole position are shown in Figure 4D, with σ_l being the standard deviation of the random disorder (expressed as a percentage of the ideal lattice spacing of 1 nm). Disorder breaks the symmetry of the lattice, which results in many additional modes gaining IR activity (with similar effects for disorder in transition dipole magnitude and orientation; see SI). This disorder-induced change of the collective vibrational spectra provides yet another degree of freedom for probing order, disorder, and crystallinity in molecular solids.

In perspective, vibrational coupling nanospectroscopy and nanoimaging provide access to low-frequency energy exchange and vibrational delocalization length, nanoscopic properties that control a wide range of macroscopic material properties. Specifically, vibrational and vibronic coupling influence photosynthetic energy transfer,^{44–46} which is limited by recombination at domain boundaries or defects. VCNC of photosynthetic systems could image changes in coupling in the vicinity of these recombination sites, thereby informing material synthesis on a more fundamental level than measurements of bulk material properties. Vibrational coupling can

also lead to self-trapping of vibrational states, which has been proposed as the energy transport mechanism in proteins and enzymes.^{5,47,48} The ability to model and measure vibrational coupling from small molecular ensembles to within single proteins can help to determine energy transfer in biological processes. VCNC and associated vibrational coupling spectroscopy can then be used to measure and image molecular disorder and vibrational delocalization, providing insights into charge and energy transfer on the fundamental length and energy scales from which these properties derive. In addition, as a collective excitation with oscillator strength borrowed from all vibrational modes of which it is composed,⁴⁹ vibrational excitons could hypothetically also serve as a carrier for quantum information.⁵⁰ Highly crystalline ensembles of small numbers of molecules could be synthesized, facilitating the preparation of single quanta of vibrations with a large amplitude. Further advancement of VCNC into nonlinear regimes or its application in multimodal approaches may lead to a new understanding of the role vibrations play in a wide range of molecular systems.

■ ASSOCIATED CONTENT

SI Supporting Information

The Supporting Information is available free of charge at <https://pubs.acs.org/doi/10.1021/acs.nanolett.3c03958>.

Additional details on sample preparation and characterization, nano-FTIR measurements, measurements of $|\mu|$, spectral fitting with Gaussian domain size distribution model, polarization dependence of collective vibrational spectra, and simulated results for model cubic lattice (PDF)

Data from X-ray diffraction measurements (PDF)

■ AUTHOR INFORMATION

Corresponding Author

Markus B. Raschke – Department of Physics and JILA, University of Colorado, Boulder, Colorado 80309, United States; orcid.org/0000-0003-2822-851X; Email: markus.raschke@colorado.edu

Authors

Richard L. Puro – Department of Physics and JILA, University of Colorado, Boulder, Colorado 80309, United States

Thomas P. Gray – Department of Physics and JILA, University of Colorado, Boulder, Colorado 80309, United States

Tsitsi A. Kapfunde – Department of Chemistry and Biochemistry, University of Oklahoma, Norman, Oklahoma 73019, United States

George B. Richter-Addo – Department of Chemistry and Biochemistry, University of Oklahoma, Norman, Oklahoma 73019, United States; orcid.org/0000-0001-9400-0113

Complete contact information is available at: <https://pubs.acs.org/doi/10.1021/acs.nanolett.3c03958>

Author Contributions

R.L.P., T.P.G., and M.B.R. designed the research; T.A.K. and G.B.R.-A. synthesized samples; T.P.G. contributed modeling tools; R.L.P. performed optical measurements, data analysis, and modeling; and R.L.P. and M.B.R. wrote the manuscript.

Notes

The authors declare no competing financial interest.

■ ACKNOWLEDGMENTS

R.L.P., T.P.G., and M.B.R. acknowledge support by the National Science Foundation (NSF) Science and Technology Center on Real-Time Functional Imaging (STROBE) under Grant DMR 1548924. T.A.K. and G.B.R. acknowledge support from the NSF under Grants CHE-1726630 and CHE-2154603, as well as the University of Oklahoma for funds to purchase the X-ray instrument and computers. The crystal structure was determined by Douglas R. Powell. We thank Roland Wilcken and Eric Muller for helpful discussions.

■ REFERENCES

- (1) Ross, M. B.; Ku, J. C.; Vaccarezza, V. M.; Schatz, G. C.; Mirkin, C. A. Nanoscale form dictates mesoscale function in plasmonic dna-nanoparticle superlattices. *Nat. Nano.* **2015**, *10*, 453–458.
- (2) Gumyusenge, A.; et al. Semiconducting polymer blends that exhibit stable charge transport at high temperatures. *Science* **2018**, *362*, 1131–1134.
- (3) Wang, Z.; et al. Disorder induced power-law gaps in an insulator–metal mott transition. *Proc. Natl. Acad. Sci. U. S. A.* **2018**, *115*, 11198–11202.
- (4) Mao, X.; et al. Self-assembled nanostructures in ionic liquids facilitate charge storage at electrified interfaces. *Nat. Mater.* **2019**, *18*, 1350–1357.
- (5) Edler, J.; Pfister, R.; Pouthier, V.; Falvo, C.; Hamm, P. Direct observation of self-trapped vibrational states in α -helices. *Phys. Rev. Lett.* **2004**, *93*, 106405.
- (6) Tiwari, V.; Peters, W. K.; Jonas, D. M. Electronic resonance with anticorrelated pigment vibrations drives photosynthetic energy transfer outside the adiabatic framework. *Proc. Natl. Acad. Sci. U. S. A.* **2013**, *110*, 1203–1208.
- (7) Nelson, T. R.; et al. Coherent exciton-vibrational dynamics and energy transfer in conjugated organics. *Nat. Commun.* **2018**, *9*, 2316.
- (8) Chin, A. W.; et al. The role of non-equilibrium vibrational structures in electronic coherence and recoherence in pigment–protein complexes. *Nat. Phys.* **2013**, *9*, 113–118.
- (9) Hestand, N. J.; Spano, F. C. Expanded theory of h-and j-molecular aggregates: the effects of vibronic coupling and intermolecular charge transfer. *Chem. Rev.* **2018**, *118*, 7069–7163.
- (10) Sneyd, A. J.; et al. Efficient energy transport in an organic semiconductor mediated by transient exciton delocalization. *Sci. Adv.* **2021**, *7*, No. eabh4232.
- (11) Dows, D. A. Intermolecular coupling of vibrations in molecular crystals. *J. Chem. Phys.* **1960**, *32*, 1342–1347.
- (12) Kasha, M. Energy Transfer Mechanisms and the Molecular Exciton Model for Molecular Aggregates. *Radiat. Res.* **1963**, *20*, 55–70.
- (13) Gray, T. P.; Nishida, J.; Johnson, S. C.; Raschke, M. B. 2D Vibrational Exciton Nanoimaging of Domain Formation in Self-Assembled Monolayers. *Nano Lett.* **2021**, *21*, 5754–5759.
- (14) Muller, E. A.; et al. Vibrational exciton nanoimaging of phases and domains in porphyrin nanocrystals. *Proc. Natl. Acad. Sci. U. S. A.* **2020**, *117*, 7030–7037.
- (15) Trzebiatowska-Gusowska, M.; Piela, K.; Misiaszek, T.; Szostak, M. M.; Baran, J. The revision of intermolecular interactions in 1,3-dinitrobenzene crystal - The role of nitro groups in optical nonlinearity. *J. Raman Spectrosc.* **2010**, *41*, 1338–1347.
- (16) Levinson, N. M.; Fried, S. D.; Boxer, S. G. Solvent-induced infrared frequency shifts in aromatic nitriles are quantitatively described by the vibrational stark effect. *J. Phys. Chem. B* **2012**, *116*, 10470–10476.
- (17) Caçado, L. G.; Beams, R.; Jorio, A.; Novotny, L. Theory of spatial coherence in near-field raman scattering. *Phys. Rev. X* **2014**, *4*, 031054.

- (18) Mueller, N. S.; et al. Collective Mid-Infrared Vibrations in Surface-Enhanced Raman Scattering. *Nano Lett.* **2022**, *22*, 7254–7260.
- (19) Beams, R.; Cançado, L. G.; Oh, S.-H.; Jorio, A.; Novotny, L. Spatial coherence in near-field raman scattering. *Phys. Rev. Lett.* **2014**, *113*, 186101.
- (20) Fried, S. D.; Boxer, S. G. Measuring electric fields and noncovalent interactions using the vibrational stark effect. *Acc. Chem. Res.* **2015**, *48*, 998–1006.
- (21) Fica-Contreras, S. M.; Charnay, A. P.; Pan, J.; Fayer, M. D. Rethinking vibrational stark spectroscopy: Peak shifts, line widths, and the role of non-stark solvent coupling. *J. Phys. Chem. B* **2023**, *127*, 717–731.
- (22) Chen, Z.; et al. Tracing the crystallization process of polyoxymethylene/poly(ethylene oxide) crystalline/crystalline blends by two-dimensional infrared correlation spectroscopy. *Vib. Spectrosc.* **2012**, *62*, 299–309.
- (23) Donges, S. A.; et al. Multidimensional nano-imaging of structure, coupling, and disorder in molecular materials. *Nano Lett.* **2021**, *21*, 6463–6470.
- (24) Signorell, R. Verification of the vibrational exciton approach for CO₂ and N₂O nanoparticles. *J. Chem. Phys.* **2003**, *118*, 2707–2715.
- (25) Sigurbjörnsson, Ó. F.; Firanescu, G.; Signorell, R. Vibrational exciton coupling as a probe for phase transitions and shape changes of fluoroform aerosol particles. *Phys. Chem. Chem. Phys.* **2009**, *11*, 187–194.
- (26) Abramavicius, D.; Zhuang, W.; Mukamel, S. Peptide secondary structure determination by three-pulse coherent vibrational spectroscopies: A simulation study. *J. Phys. Chem. B* **2004**, *108*, 18034–18045.
- (27) Gorbunov, R. D.; Kosov, D. S.; Stock, G. Ab initio-based exciton model of amide I vibrations in peptides: Definition, conformational dependence, and transferability. *J. Chem. Phys.* **2005**, *122*, 224904.
- (28) Malolepsza, E.; Straub, J. E. Empirical maps for the calculation of amide I vibrational spectra of proteins from classical molecular dynamics simulations. *J. Phys. Chem. B* **2014**, *118*, 7848–7855.
- (29) Reppert, M.; Tokmakoff, A. Electrostatic frequency shifts in amide I vibrational spectra: Direct parameterization against experiment. *J. Chem. Phys.* **2013**, *138*, 134116.
- (30) Kobayashi, M.; Sakashita, M. Morphology dependent anomalous frequency shifts of infrared absorption bands of polymer crystals: Interpretation in terms of transition dipole-dipole coupling theory. *J. Chem. Phys.* **1992**, *96*, 748–760.
- (31) Moran, A.; Mukamel, S. The origin of vibrational mode couplings in various secondary structural motifs of polypeptides. *Proc. Natl. Acad. Sci. U. S. A.* **2004**, *101*, 506–510.
- (32) La Cour Jansen, T.; Dijkstra, A. G.; Watson, T. M.; Hirst, J. D.; Knoester, J. Modeling the amide I bands of small peptides. *J. Chem. Phys.* **2006**, *125*, 044312.
- (33) Tanabe, Y.; Shimomura, M. A₂Mode Vibration in Infrared Absorption Spectrum of Trigonal Poly(oxymethylene). *Macromolecules* **1990**, *23*, 5031–5034.
- (34) Hamm, P.; Zanni, M. *Concepts and methods of 2D infrared spectroscopy*; Cambridge University Press: Cambridge, UK, 2012.
- (35) Muller, E. A.; Pollard, B.; Raschke, M. B. Infrared chemical nano-imaging: Accessing structure, coupling, and dynamics on molecular length scales. *J. Phys. Chem. Lett.* **2015**, *6*, 1275–1284.
- (36) Lee, J.; Twamley, B.; Richter-Addo, G. B. Nitrones are suitable ligands for heme models: X-ray crystal structure of the first metalloporphyrin nitron complex. *Chem. Commun.* **2002**, 380–381.
- (37) Andrews, S. S.; Boxer, S. G. Vibrational stark effects of nitriles. i. methods and experimental results. *J. Phys. Chem. A* **2000**, *104*, 11853–11863.
- (38) Atkins, P. *Physical Chemistry*, 5th ed.; W. H. Freeman and Company: New York, NY, 1994).
- (39) Muller, E. A.; Pollard, B.; Bechtel, H. A.; van Blerkom, P.; Raschke, M. B. Infrared vibrational nanocrystallography and nano-imaging. *Sci. Adv.* **2016**, *2*, No. e1601006.
- (40) Govyadinov, A. A.; Amenabar, I.; Huth, F.; Carney, P. S.; Hillenbrand, R. Quantitative measurement of local infrared absorption and dielectric function with tip-enhanced near-field microscopy. *Journal of physical chemistry letters* **2013**, *4*, 1526–1531.
- (41) Ohta, T.; et al. Interlayer interaction and electronic screening in multilayer graphene investigated with angle-resolved photoemission spectroscopy. *Phys. Rev. Lett.* **2007**, *98*, 206802.
- (42) Wang, L.; et al. Quadrupole contribution of C=O vibrational band in sum frequency generation spectra of organic carbonates. *J. Phys. Chem. Lett.* **2020**, *11*, 8527–8531.
- (43) Pollard, B.; Muller, E. A.; Hinrichs, K.; Raschke, M. B. Vibrational nano-spectroscopic imaging correlating structure with intermolecular coupling and dynamics. *Nat. Commun.* **2014**, *5*, 1–7.
- (44) Tiwari, V.; Peters, W. K.; Jonas, D. M. Electronic resonance with anticorrelated pigment vibrations drives photosynthetic energy transfer outside the adiabatic framework. *Proc. Natl. Acad. Sci. U. S. A.* **2013**, *110*, 1203–1208.
- (45) Yeh, S.-H.; Hoehn, R. D.; Allodi, M. A.; Engel, G. S.; Kais, S. Elucidation of near-resonance vibronic coherence lifetimes by nonadiabatic electronic-vibrational state character mixing. *Proc. Natl. Acad. Sci. U. S. A.* **2019**, *116*, 18263–18268.
- (46) Higgins, J. S.; et al. Photosynthesis tunes quantum-mechanical mixing of electronic and vibrational states to steer exciton energy transfer. *Proc. Natl. Acad. Sci. U. S. A.* **2021**, *118*, No. e2018240118.
- (47) Davydov, A. S. The theory of contraction of proteins under their excitation. *J. Theor. Biol.* **1973**, *38*, 559–569.
- (48) Schwartz, E.; et al. Self-trapped vibrational states in synthetic β -sheet helices. *Chem. Commun.* **2009**, 4675–4677.
- (49) Pouthier, V. Vibrational exciton mediated quantum state transfer: Simple model. *Phys. Rev. B* **2012**, *85*, 214303.
- (50) Tesch, C. M.; de Vivie-Riedle, R. Quantum computation with vibrationally excited molecules. *Physical review letters* **2002**, *89*, 157901.